Chapter 4
Water Research by Far-Ultraviolet Spectroscopy

Takeyoshi Goto and Akifumi Ikehata

Abstract Far-ultraviolet (FUV) absorption spectroscopy provides molecular information about valence electronic transitions: σ, n, and π electron excitation and charge transfer (CT). FUV spectral measurements of liquid water and aqueous solutions had been limited, because the absorptivity of liquid water is very intense (absorptivity 10^5 cm^{-1} at 150 nm). We have developed an attenuated total reflection (ATR)-type FUV spectrophotometer in order to measure FUV spectra of liquid water and aqueous solutions. The ATR–FUV spectroscopy reveals the features of the valence electronic transition of liquid water. This chapter introduces a brief overview of the first electronic transition $\left(\tilde{A} \leftarrow \tilde{X} \right)$ of liquid water (Sect. 4.1) and the FUV spectral analyses (140–300 nm) of various aqueous solutions including how the hydrogen bonding interaction of liquid water affects the $\tilde{A} \leftarrow \tilde{X}$ transition of water molecules (Sect. 4.1); how the $\tilde{A} \leftarrow \tilde{X}$ bands of water molecules in Groups I, II, XIII, and lanthanoid (Ln^{3+}) electrolyte solutions are associated with the hydration states of the metal cations (Sects. 4.2 and 4.3) how the protonation states of amino acids in aqueous solutions affect the electronic transition of the amino acids (Sect. 4.4) and the analysis of O$_3$ pulse-photolytic reaction in aqueous solution using a nanosecond pump-probe transient FUV spectrophotometer (Sect. 4.5).

Keywords Far ultraviolet (FUV) • Attenuated total reflection (ATR) • Liquid water • Hydrogen bond • Hydration • Electrolyte solution • Amino acids • Aqueous ozone photolysis

T. Goto

Department of Chemistry, School of Science and Technology, Kwansei Gakuin University, 2-1 Gakuen, Sanda 669-1337, Japan

A. Ikehata (✉)

National Food Research Institute, National Agriculture and Food Research Organization, (NARO), 2-1-12 Kannondai, Tsukuba, Ibaraki 305-8642, Japan
e-mail: ikehata@affrc.go.jp

4.1 First Electronic Transition of Liquid Water

Water is a colorless medium; it does not absorb visible light, while infrared (IR) and far-ultraviolet (FUV) light is strongly absorbed. Figure 4.1 shows the absorption spectrum of liquid water from the IR to the FUV region calculated from literature data of molar absorptivities [1] by assuming a path length of 100 nm. In the IR region, two major peaks appear around 2,900 nm (3,400 cm^{-1}) and 6,200 nm (1,650 cm^{-1}) assigned to H–O–H stretching and bending modes, respectively. In the near-infrared (NIR) region, relatively small absorptions due to the overtones and combination modes of the H–O–H vibrations are observed. As mentioned at the beginning, the ultraviolet–visible (UV-vis) region does not show significant absorption. In the FUV region, a strong absorption band arises where the wavelength is shorter than 190 nm. This is the first electronic transition of water, and the absorptivity of this band is stronger by several orders of magnitude relative to the H–O–H stretching band in the IR region. For decades, it has been known that the absorption edge of this band (around 190 nm) shifts to a shorter wavelength with the increase in the strength of hydrogen bonding [2–5]. This band is simply called the $\tilde{A} \leftarrow \tilde{X}$ because it is due to the lowest electronic transition. Specifically, this band is assigned to the transitions from the $1b_1$ (nonbonding orbital) to the $4a_1$ (antibonding σ* orbital) and partly to the 3s orbitals (Fig. 4.2) [6, 7]. Since the former $1b_1 \rightarrow 4a_1$ is caused by a transition to valence band of the oxygen atom, the $\tilde{A} \leftarrow \tilde{X}$ absorption of water has an aspect of an excitonic transition [8]. In condensed phases, the lone-pair valence band edge approaches the conduction band. Hahn et al. clarified that the average electron-hole distance is longer in the condensed phase than in
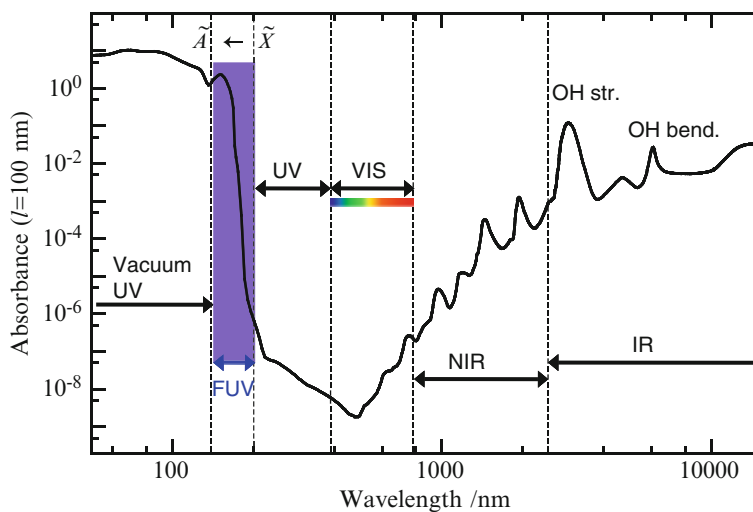

Fig. 4.1 The absorbance spectrum of water from the IR to FUV region, assuming a path length of 100 nm (From Ref. [1])

Excited state

$(1a_1)^2$ $(2a_1)^2$ $(1b_2)^2(3a_1)^2(1b_1)(3s/4a_1)$

Ground state

$(1a_1)^2$ $(2a_1)^2$ $(1b_2)^2(3a_1)^2(1b_1)^2$
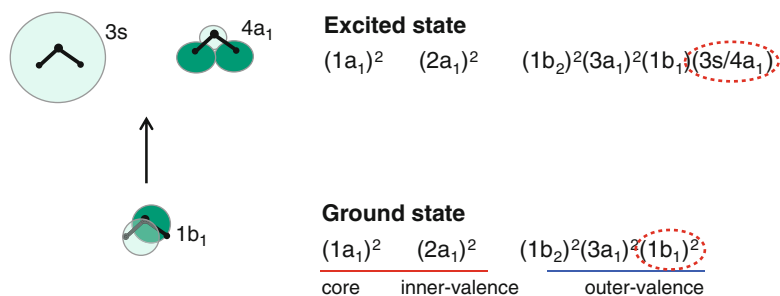
core   inner-valence   outer-valence

Fig. 4.2 Molecular orbitals of water molecule in the ground state and the first excited states

an isolated water molecule by theoretical calculations [9]. This result supports the experimentally observed blueshifts of $\tilde{A} \leftarrow \tilde{X}$. The latter $1b_1 \rightarrow 3s$ is a transition to the Rydberg series, often called molecular orbital (MO) Rydbergization [6, 10]. The radii of the electron orbitals of Rydberg states are several to several tens of times larger than those of the corresponding ground state, so that the Rydberg states in condensed phases are sensitive to the effects of surrounding molecules. The obvious blueshift that was experimentally observed for matrix-isolated water with a decrease in the size of the matrix constituents represented a proof for Rydbergization [11]. Actually the excited states of valence and Rydberg orbitals are complementary by the O–H distances. When the O–H distance becomes shorter (i.e., in condensed phase), Rydberg nature of the excited molecular orbital becomes dominant [10].

From the peak shifts of the $\tilde{A} \leftarrow \tilde{X}$ band by phase transitions of water, one can easily understand the fact that the first electronic transition of water varies with changes in hydrogen bonding and molecular density. The band maxima of $\tilde{A} \leftarrow \tilde{X}$ of water are observed at 168 nm (7.4 eV) [12, 13], 148–150 (8.4–8.3 eV) [14–18], and 144 nm (8.6 eV) [18–20] for the gas, liquid, and solid states, respectively. However, the $\tilde{A} \leftarrow \tilde{X}$ absorption of water is considerably stronger than the IR absorptions corresponding to the fundamental H–O–H stretching vibrations as shown in Fig. 4.1, and this fact makes it difficult to measure the band maxima of the $\tilde{A} \leftarrow \tilde{X}$ absorption of liquid water and aqueous solutions by transmittance spectroscopy. In fact, the positions of the band maxima of liquid water and ice mentioned in the foregoing researches [11, 15] were determined by regular reflection measurements. As for liquid water and aqueous solutions, many other scientists had to observe the band tail over 190 nm (below 6.5 eV) by using transmittance cells and have discussed the onset of the absorption [2–5, 8]. A redshift occurs at the onset of the $\tilde{A} \leftarrow \tilde{X}$ absorption with an increase of temperature [8, 21, 22]. This phenomenon has been discussed in the context of Urbach rule [23], which is based on the characteristic behavior of phonon-broadened absorption bands. Williams et al. compared the energy gap for the $\tilde{A} \leftarrow \tilde{X}$ band of liquid water with that of the band of isolated water from a viewpoint of an amorphous semiconductor on the basis of temperature dependence measurements of UV spectra [8]. The studies conducted before 1998 were adequately reviewed by

Bernas [22, 24]. Considerable computational efforts were also made recently [25–32]. However, experimental study of the $\tilde{A} \leftarrow \tilde{X}$ absorption of liquid water had not been fully explored due to the difficulty in directly observing the transmittance FUV spectra of water. The situation has dramatically changed by the development of ATR–FUV spectroscopy [33]. One can easily observe the entire shape of the $\tilde{A} \leftarrow \tilde{X}$ absorption band of water because the evanescent wave with the ATR geometry reduces a path length in the sample on the reflection element less than 100 nm. Since the $\tilde{A} \leftarrow \tilde{X}$ band moves to a shorter wavelength with the increase in the strength of hydrogen bonding, it is expected that the $\tilde{A} \leftarrow \tilde{X}$ band of liquid water continuously shifts with temperature and hydration by ions, inorganic molecules, and organic molecules. The use of $\tilde{A} \leftarrow \tilde{X}$ band by ATR–FUV spectroscopy is now becoming a method to explore the hydrogen bonding and hydration of water and also a method in quantitative and qualitative analysis of aqueous solutions [34].

The origin of the low-lying electronic transition band of water had not been conclusively established before the development of the ATR–FUV because the observation of the $\tilde{A} \leftarrow \tilde{X}$ band tail was the only one way to know the electronic property. To make sure whether the shift of the $\tilde{A} \leftarrow \tilde{X}$ band tail by heating is caused by broadening or energy shift, the ATR–FUV was first used for studying temperature dependence on the $\tilde{A} \leftarrow \tilde{X}$ transition by employing a single-reflection ATR accessory with a sapphire crystal [14]. The ATR–FUV spectra of light water (H$_2$O) and heavy water (D$_2$O) measured at different temperatures (10–70 °C) are shown in Fig. 4.3. The maximum absorptions for all the spectra of D$_2$O lie at higher energies than those for the spectra of H$_2$O at the same temperature. The
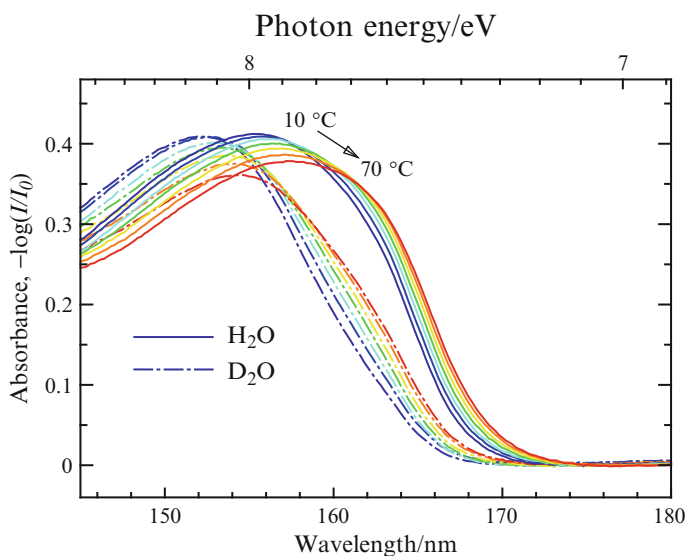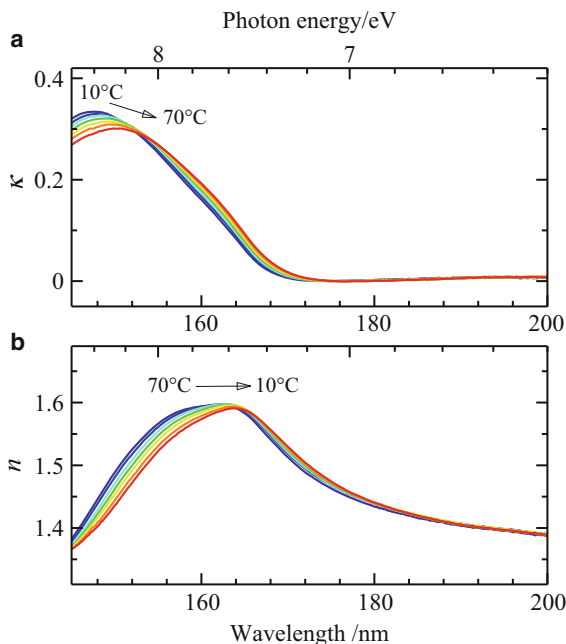

Fig. 4.3 ATR–FUV spectra (ATR absorbance) of H$_2$O and D$_2$O at different temperatures (From Ref. [14])

Fig. 4.4 The absorption index κ (**a**) and the refractive indices n (**b**) of H_2O converted from the ATR–FUV spectra shown in Fig. 4.3 by the Kramers–Kronig transformation (From Ref. [14])

deviation arises from the difference in the vibrational zero-point energies between H_2O and D_2O [17]. The $\tilde{A} \leftarrow \tilde{X}$ peaks showmarked redshifts on heating, and the peak intensities decrease. However, the ATR spectra of water are not identical to its transmission spectra. Since the ATR technique is based upon a reflection method, the spectra involve shifts not only in peak intensity but also in the wavelength. Kramers–Kronig transformation (KKT) and Fresnel formulas are available to separate the contributions of the absorption and refractive indices. Figure 4.4a, b displays the calculated results of absorption indices, κ, and refractive indices, n, of H_2O, respectively [14]. The indices correspond to the real and imaginary parts of the complex refractive index as follows: $\tilde{n} = n + i\kappa$. It can be seen that every spectrum of the optical indices shifts to the low-energy side on heating. The peak wavelengths of the absorption indices are plotted against temperature in Fig. 4.5. The best-fit linear functions to the data are indicated by solid lines. The band maximum of H_2O linearly shifts from 8.4 to 8.26 eV on increasing the temperature from 10 to 70 °C, and consequently, the slope is -2.4×10^{-3} eV/K. A prediction by using an extrapolation fit of a Gaussian profile to the experimentally observed UV tails shows a smaller slope of -1.86×10^{-3} [5]. The slope for D_2O, -2.1×10^{-3} eV/K, is thought to be the same as that for H_2O. This result suggests that with regard to the thermal shifts of the band peaks, the ATR–FUV spectra are relatively in good agreement with the transmittance spectra. On the other hand, the bandwidth of the $\tilde{A} \leftarrow \tilde{X}$ band in the absorption indices, κ, becomes very slightly narrow with an increase in the temperature. Therefore, it is revealed that the shift of the tail of $\tilde{A} \leftarrow \tilde{X}$ absorption observed in the UV spectra is dominated by the energy shift

Fig. 4.5 Plots of the peak positions of the $\tilde{A} \leftarrow \tilde{X}$ band for H_2O (*open circles*) and D_2O (*filled circles*) against temperature (From Ref. [14])
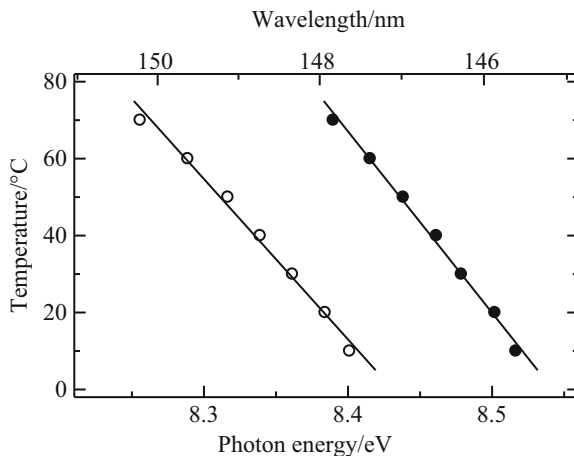
of the $\tilde{A} \leftarrow \tilde{X}$ transition. In this way, systematic measurements of the ATR–FUV spectra of water and the analysis of KKT reveal that the $\tilde{A} \leftarrow \tilde{X}$ band of liquid water shifts to lower energy on heating.

4.2 Cationic Effects on the $\tilde{A} \leftarrow \tilde{X}$ Transition of Liquid Water: Group I, II, and XIII Cations

Because the $\tilde{A} \leftarrow \tilde{X}$ transition of liquid water involves nonbonding electrons of an oxygen atom of a water molecule [6], the $\tilde{A} \leftarrow \tilde{X}$ transition of liquid water is sensitively affected by the hydrogen bonding state of water molecules. The addition of salts in liquid water induces the rearrangement of the hydrogen bonding structure, and the strength of water molecule structuring by an ion is characterized with the charge and the size of the ion [35, 36]. The high-charge-density ions electrostatically bind to the surrounding water molecules and form the first and even second coordination spheres [37]. The hydration energy of an ion expresses the change of the electric energy induced by the insertion of an ion into water solvent. Hydration of ions has been extensively studied from the macroscopic properties (viscosity and entropy of ion solvation) [38, 39] and the molecular structure with X-ray [40], nuclear magnetic resonance (NMR) [41], and vibrational [42] spectroscopy. Herein, ATR–FUV spectroscopy provides new insights into the hydration of cations from the perspective of the electronic transition of water molecules [43, 44].

The $\tilde{A} \leftarrow \tilde{X}$ transition energy of liquid water increases with the addition of salts, and the increase in the energy linearly correlates with the thermodynamic solvation energies of the cations [43, 44]. Figure 4.6 shows the ATR–FUV spectra of 1 M Group I metal nitrate solutions and pure water at 25 °C. The same counter-anion, nitrate, was employed for all the electrolyte solutions to negate the effect of counter-
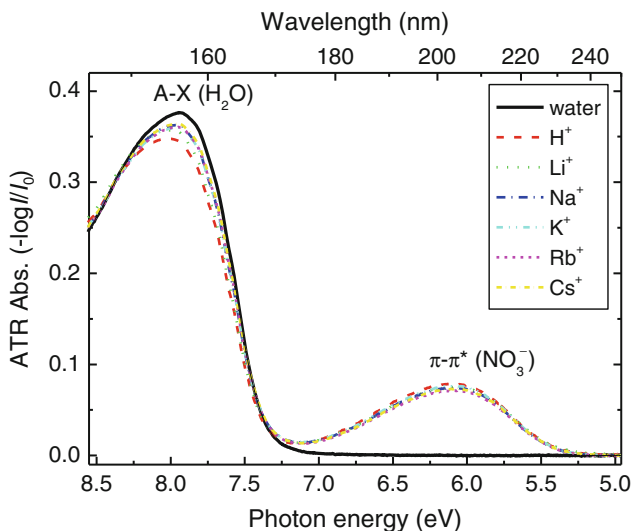
Fig. 4.6 ATR–FUV spectra of aqueous solutions of 1 M alkali metal nitrates measured at 25 °C (From Ref. [43])

anions on the measured spectra. The absorption bands around 6.1 eV (203 nm) and 8.0 eV (155 nm) are assigned to the $\pi - \pi^*$ transition of NO_3^- and the $\tilde{A} \leftarrow \tilde{X}$ transition of water molecules, respectively. The $\tilde{A} \leftarrow \tilde{X}$ bands of the electrolyte solutions are slightly blueshifted, and their absorbances are smaller relative to the pure water band. The $\tilde{A} \leftarrow \tilde{X}$ transition energies of the electrolyte solutions become higher as the cation sizes are smaller in each group. Figure 4.7 shows plots of the barycenter energies of the $\tilde{A} \leftarrow \tilde{X}$ bands of the Group I, II, and XIII metal nitrate electrolyte solutions (1 M) versus the Gibbs hydration energies of the cations (ΔG_{hyd}). The ΔG_{hyd} values were taken from the reference [45]. Because the concentrations of the nitrate anion are different among the Groups I, II, and XIII, the correlation can be examined within each group. The higher-charge-density cations which hold the larger negative values of ΔG_{hyd} show the higher $\tilde{A} \leftarrow \tilde{X}$ transition energies of the water molecules for each group. This linear relation indicates that the hydration of the cations stabilizes the ground-state electronic energies of the water molecules, resulting in the increase in the $\tilde{A} \leftarrow \tilde{X}$ transition energies of the electrolyte solutions. The correlations of the extremely high-charge-density cations, H^+, Li^+, and Be^{2+}, deviate from the linear relations. This deviation is probably attributed to the energy differences in the electronic excited state of the water molecules hydrating different cations, because the thermodynamic hydration energy of a cation is associated with the ground-state electronic energy. The electronic state calculation of the hexagonal ice water shows that the spatial distribution of the excited electrons is extensively distributed and sensitive to the neighboring molecular environment [9]. Therefore, the extremely
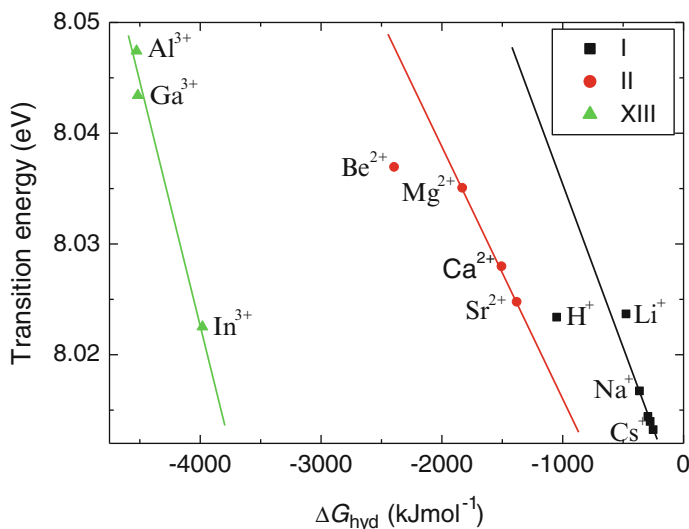
Fig. 4.7 Plot of the $\tilde{A} \leftarrow \tilde{X}$ transition energies of Group I, II, and XIII electrolyte solutions versus the Gibbs energies of hydration (ΔG_{hyd}) corresponding the cations. The ΔG_{hyd} values were taken from the reference [45] (From Ref. [43])

high-charge-density cations more strongly perturb the molecular orbital (MO) transformation of a water molecule accompanied with the electronic transition than the low-charge-density cations.

The electronic state calculations of water and water–cation complexes reveal how the electron donation from water molecules to a metal cation affects the $\tilde{A} \leftarrow \tilde{X}$ transition of the water molecules [43]. The time-dependent density-functional theory (TDDFT) calculations of the $\tilde{A} \leftarrow \tilde{X}$ transitions of the monomer and the dimer of water molecules (*mono*-H_2O and *di*-H_2O) and the water-monovalent cation complexes (H_2O-M^+) using the M06-2X functional with the 6-31++G** basis set show a clear dependence of the $\tilde{A} \leftarrow \tilde{X}$ transition energy on distance between the electron donor (nonbonding electrons of an oxygen atom) and the acceptor (M^+ or a hydrogen atom of a water molecule) (r_{D-A}) as shown in Fig. 4.8. The longest and shortest r_{D-A} distances of each cation complex correspond with the inner and outer positions of the first hydration shell edges of the cations. As r_{D-A} is shorter, the $\tilde{A} \leftarrow \tilde{X}$ transition energies of all the cation complexes and *di*-H_2O (b) become larger than that of the water monomer. The *di*-H_2O (a) transition appears below the *mono*-H_2O. But the oscillator strength of the *di*-H_2O (a) transition gets smaller as r_{D-A} is shorter, whereas that of the *di*-H_2O (b) transition doesn't change. From the results of these TDDFT calculations, the blueshifts of the $\tilde{A} \leftarrow \tilde{X}$ bands of the electrolyte solutions can be elucidated as the following: (1) The electron donor–acceptor interaction between the cations and the water molecules induces deformation of the MO of the water molecules, and (2) a closed-packing hydrogen bonding structure of the water molecules caused by the electric fields of the cations generates the stronger
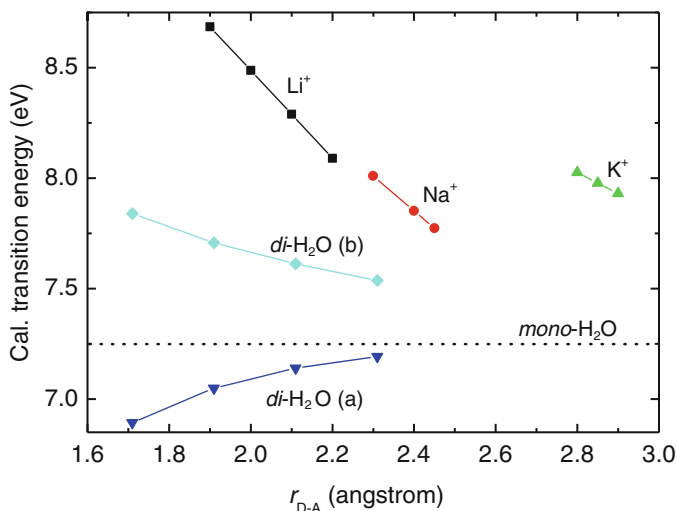
Fig. 4.8 The $\tilde{A} \leftarrow \tilde{X}$ transition energies for the H_2O dimer (*di*-H_2O (*a*) and *di*-H_2O (*b*)), H_2O-Li^+, H_2O-Na^+, and H_2O-K^+ complexes calculated by M06-2X/6-31++G** at various r_{D-A} distances. The longest and shortest r_{D-A} distances correspond with the lengths between the inner and outer positions of the hydration shell edges of each cation. The *broken line* shows the $\tilde{A} \leftarrow \tilde{X}$ transition energy of the H_2O monomer (From Ref. [43])

hydrogen bond interaction among the water molecules. Consequently, the $\tilde{A} \leftarrow \tilde{X}$ bands of the high-charge-density cation electrolyte solutions are more blueshifted than those of the low-charge-density electrolyte solutions and pure water. Also, the calculated $\tilde{A} \leftarrow \tilde{X}$ transition energy spread between the longest and shortest r_{D-A} distances of the H_2O-M^+ complexes linearly correlates with the full with at half maximums of the $\tilde{A} \leftarrow \tilde{X}$ bands of the electrolyte solutions measured with ATR–FUV spectroscopy as shown in Fig. 4.9. Therefore, the $\tilde{A} \leftarrow \tilde{X}$ bandwidths of the electrolyte solutions directly exhibit how the cation centers are hydrated by the solvent water molecules.

4.3   Cationic Effects on the $\tilde{A} \leftarrow \tilde{X}$ Transition of Liquid Water: Lanthanoid Cations

Physicochemical properties of lanthanoid cation (Ln^{3+}) hydrates depend on the 4f electron occupation state of the Ln^{3+} cations in the electronic [46, 47] and electric aspects [48]. Accordingly, those vary across the 4f period in either monotonous or inmonotonous trend. As the nuclear charge (*Z*) increases, the coordination number of Ln^{3+} hydrates decreases inmonotonously from 9 to 8; specifically, the amount of change varies around Eu^{3+} and Gd^{3+} [48–50]. The Ln–OH_2 bond distances

Fig. 4.9 Plot of the calculated $\tilde{A} \leftarrow \tilde{X}$ transition energy spreads for the widths of hydration shells versus the full width at half maximums (FWHM) of the $\tilde{A} \leftarrow \tilde{X}$ bands measured with ATR–FUV spectroscopy. The *broken line* shows the FWHM of the $\tilde{A} \leftarrow \tilde{X}$ band of pure water (From Ref. [43])
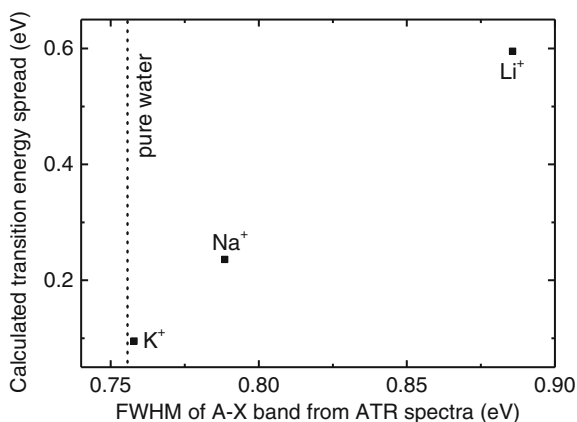
monotonously decrease [51–53], and the Gibbs energies of hydration of Ln^{3+} cations monotonously increase [45, 54], as the Z values become large. The variation of the lanthanoid liquid–liquid extraction with Z shows a characteristic tetrad trend [55]. The tetrad trends of Ln^{3+} hydrates are known as the tetrad effects [46, 47]. Herein, ATR–FUV spectroscopy reveals that the $\tilde{A} \leftarrow \tilde{X}$ transition energies of the Ln^{3+} electrolyte solutions show a tetrad trend across the 4f period, which accounts for the ligand field splitting (LFS) of the 4f electronic states of the Ln^{3+} hydrates [56].

The $\tilde{A} \leftarrow \tilde{X}$ transition energies of the Ln^{3+} electrolyte solutions are higher than that of pure water. Figure 4.10 shows the plots of the $\tilde{A} \leftarrow \tilde{X}$ transition energies of the Ln^{3+} and the Group XIII nitrate electrolyte solutions (1 M) versus the Gibbs energies of hydration (ΔG_{hyd}) of each cation. The ΔG_{hyd} values were taken from the reference [45]. Because the same counter-anion (nitrate) for all the salts was employed, the spectral differences are attributed to the cation effects. From the linear correlation, the hydration energies of the Group XIII cations account for the decrease in the electronic energies of the ground state of the water molecules and the increases in the $\tilde{A} \leftarrow \tilde{X}$ transition energies of the Group XIII electrolyte solutions. In contrast, the $\tilde{A} \leftarrow \tilde{X}$ transition energies of all the Ln^{3+} electrolyte solutions including the noble gas-like cation La^{3+} ([Xe]$4f^0$) do not have a linear relation with ΔG_{hyd}. Because the cations in each Group I, II, or XIII (s- and p-block metals) exhibit a linear relation as shown in the previous section, the deviation from the linearity for the Ln^{3+} cations is associated with the 4f electronic states.

The 4f electron occupation state can characterize the $\tilde{A} \leftarrow \tilde{X}$ transition energies of the Ln^{3+} electrolyte solutions in a tetrad manner; that is, there are four local trends in the 4f series. Figure 4.11 shows a plot of the $\tilde{A} \leftarrow \tilde{X}$ transition energies (filled squares, left axis) and ΔG_{hyd} (filled circles, right axis) versus the number of 4f electrons of the Ln^{3+} cations. For the half occupation period of the 4f electrons, the $\tilde{A} \leftarrow \tilde{X}$ transition energies decrease from La^{3+} ($4f^0$, 8.0375 eV) to Nd^{3+} ($4f^3$, 8.0277 eV) and increase from Sm^{3+} ($4f^5$, 8.0279 eV) to Gd^{3+} ($4f^7$, 8.0374 eV). For the complete occupation period, there are two local minima at Dy^{3+} ($4f^9$,
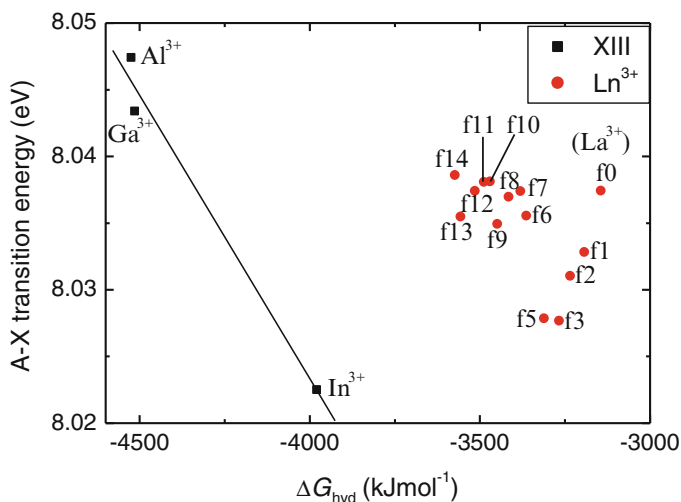
Fig. 4.10 Plots of the $\tilde{A} \leftarrow \tilde{X}$ transition energies of Ln^{3+} and Group XIII electrolyte solutions versus the Gibbs energies of hydration (ΔG_{hyd}) for the corresponding cations. The ΔG_{hyd} values were taken from the reference [45] (From Ref. [56])
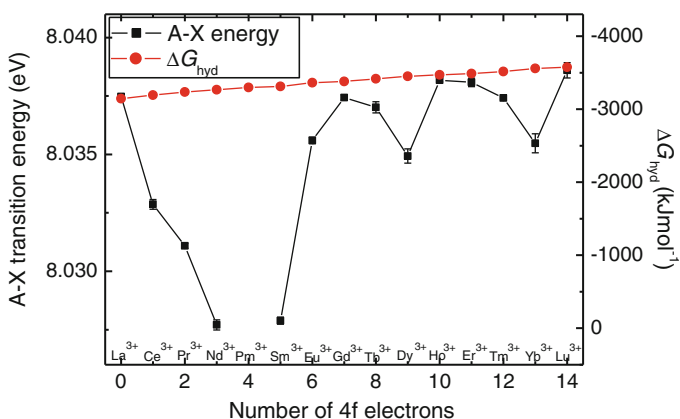

Fig. 4.11 Plot of the $\tilde{A} \leftarrow \tilde{X}$ transition energies (*filled squares, left axis*) and ΔG_{hyd} (*filled circles, right axis*) versus the number of 4f electrons of the Ln^{3+} cations. The ΔG_{hyd} values were taken from the reference [45] (From Ref. [56])

8.0349 eV) and Yb^{3+} ($4f^{13}$, 8.0355 eV). The $\tilde{A} \leftarrow \tilde{X}$ transition energies at the nodes (La^{3+}, Gd^{3+}, Ho^{3+}, and Lu^{3+}) slightly increase as Z increases from La^{3+} (8.0374 eV) to Gd^{3+} (8.0374 eV) and Ho^{3+} (8.0382 eV) to Lu^{3+} (8.0386 eV). Consequently, the primary trend of the $\tilde{A} \leftarrow \tilde{X}$ transition energies of the Ln^{3+} electrolyte solutions is a linear relation with the hydration energies of the Ln^{3+} cations, and that is the same as the Group I, II, and XIII cations.
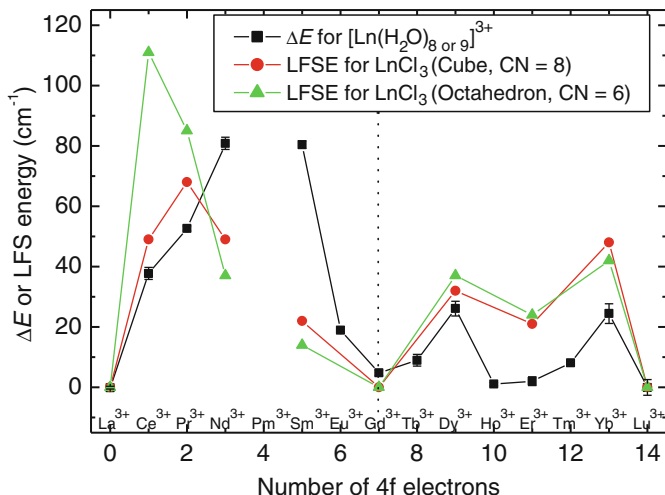
Fig. 4.12 The differences (ΔE, *filled squares*) between the measured $\tilde{A} \leftarrow \tilde{X}$ transition energies and the line between La^{3+} and Lu^{3+} and the LFS energy of the $LnCl_3$ crystals at the vertices of a cube (CN = 8, *filled circles*) and an octahedron (CN = 6, *filled triangles*) from Ref. [58] (From Ref. [56])

   The difference of the $\tilde{A} \leftarrow \tilde{X}$ transition energy of each Ln^{3+} from the line, which goes through the nodes, (ΔE), more clearly characterizes the tetrad trend deviation. Figure 4.12 shows the plots of ΔE across the 4f period. For the half occupation period, the ΔE value increases from La^{3+} to Nd^{3+} (9.98×10^{-3} eV, 80.5 cm^{-1}) and decreases from Sm^{3+} (9.97×10^{-3} eV, 80.4 cm^{-1}) to Gd^{3+} (5.99×10^{-4} eV, 4.83 cm^{-1}). For the complete occupation period, the ΔE shows the local maxima at Dy^{3+} (3.24×10^{-3} eV, 26.1 cm^{-1}) and Yb^{3+} (3.03×10^{-3} eV, 24.5 cm^{-1}) and the local minimum between Ho^{3+} and Er^{3+}.

   The tetrad trend of ΔE across the 4f period is ascribed to the LFS effect on the inner 4f electrons of the Ln^{3+} cations. The observed ΔE values are the comparable order of magnitude with the splitting ground-state multiplets of Ln^{3+} complexes induced by ligand fields in the range from 0 to 400 cm^{-1} [57–64]. From the electronic state calculation with INDO/S-CI method, the energy split is from 0 to 263 cm^{-1} for $[Pr(H_2O)_9]^{3+}$ complex (D_{3h} symmetry) and from 0 to 196 cm^{-1} for $[Tm(H_2O)_8]^{3+}$ complex (D_{2d} symmetry) [64]. Also, the observed ΔE profile along the 4f period is similar with the LFS profile of the ground-state multiplets of the cube geometry (coordination number (CN) = 8) rather than the octahedron geometry (CN = 6) of the Ln^{3+} halides crystals. Yatsimirskii et al. calculated the ground-state multiplets of the Ln^{3+} halide crystals [14]. The calculated LFS energies for the cube (filled circle) and the octahedron (filled triangle) geometry of a $LnCl_3$ crystal by Yatsimirskii et al. are also plotted in Fig. 4.12. The molecular geometry of Ln^{3+} hydrates in aqueous solution is tricapped trigonal prism (CN = 9) for light elements and square antiprism (CN = 8) for heavy elements [50–52, 65]. The LFS profiles

for those geometries of the Ln^{3+} hydrates are not known at this time. However, the similarity of the ΔE profile with the LFS profile of the cube (CN = 8) geometry rather than octahedron (CN = 6) of the Ln^{3+} halides indicates that the tetrad trend of ΔE results from the LFS of the ground-state multiplets of the Ln^{3+} hydrates.

4.4 Electronic Transitions of Amino Acids in Aqueous Solutions

Amino acids are simple building-block subunits of proteins, and their side chains determine the higher-order structures and the chemical functions of proteins. The FUV spectral measurements of amino acids especially in gas and solution states are very challenging, because the vapor pressures of amino acids are quite low [66], and the photoabsorption of solvents including water is very intense [7, 14]. Just a few FUV absorption spectra of amino acids were reported in the thin solid films [67, 68], the gas states [69, 70], and the solution states [71, 72]. Actually, the FUV spectra of amino acids in aqueous solutions can be easily obtained by using the ATR method. This section will introduce the FUV spectra of 20 naturally occurring amino acids in pure water, acidic, and basic aqueous solutions in the region from 145 to 300 nm [73].

Glycine (Gly) is the simplest molecule in the 20 amino acids, and the FUV spectrum of Gly is the most appropriate to show the electronic transition of the backbone structure of amino acids. The primary chromophore of Gly is the carboxyl group. Figure 4.13 shows the FUV spectra of 2 M Gly in 1.81 M H_2SO_4, pure water, and 3.36 M NaOH aqueous solutions. Because the pK_{a1} and pK_{a2} values of Gly are 2.34 and 9.60, the protonation states are ammonium carboxylic acid, zwitterion, and aminocarboxylate anion in acidic solution, pure water, and basic solution, respectively. The intense bands appear at 157.5 nm (molar absorption coefficient $\varepsilon = 5.15 \times 10^3$ M^{-1} cm^{-1}), 168.9 nm (7.76×10^3 M^{-1} cm^{-1}), and 169.9 nm (7.73×10^3 M^{-1} cm^{-1}) for the acid, the zwitterion, and the anion forms, respectively. Those are assigned to the $(\pi - \pi^*)_1$ transitions of the carboxyl and the carboxylate groups. In accordance with the conversion from the acid form to the zwitterion, the $(\pi - \pi^*)_1$ band is redshifted by 11.4 nm, the maximum ε value increases by 2.61×10^3 M^{-1} cm^{-1}, and the new band appears at 145.8 nm (5.77×10^3 M^{-1} cm^{-1}) which is tentatively denoted as $(\pi - \pi^*)_2$. The $(\pi - \pi^*)_2$ band of the carboxylate anion form was reported from the quantum chemical calculations of electronic transition and circular dichroism (CD) of hydrated alanine (Ala) [74, 75] and the absorption spectra of the amino acid solid films [67, 68]. Osted et al. reported that the electronic transition energies of the $(\pi - \pi^*)_1$ and $(\pi - \pi^*)_2$ bands are around 170 and 149 nm for the micro-hydrated zwitterion form of Ala from the coupled cluster singles and doubles (CCSD) level calculations [75]. In conversion from the zwitterion form to the anion, the $(\pi - \pi^*)_1$ band is slightly redshifted by 1 nm, and the $(\pi - \pi^*)_2$ band becomes indistinguishably smaller.
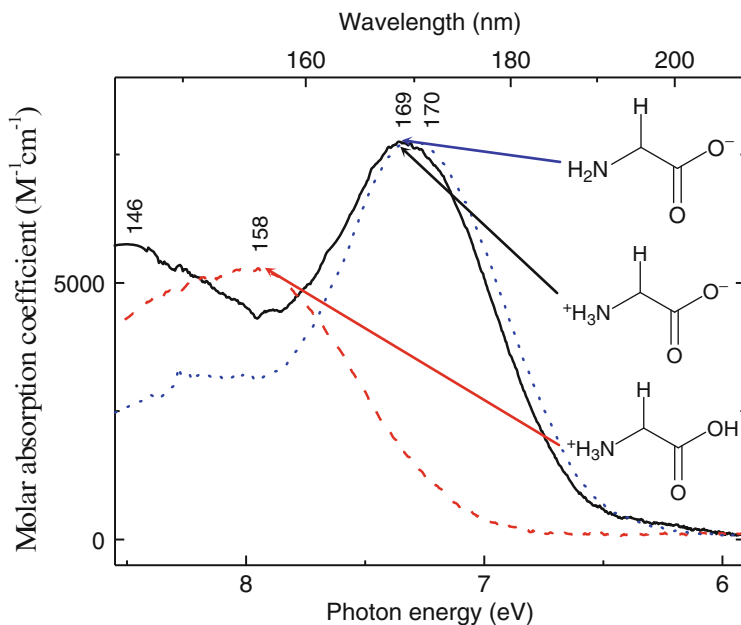
Fig. 4.13 FUV absorption spectra of 2 M Gly in the protonated, zwitterion, and deprotonated forms (From Ref. [73])

Accordingly, the $(\pi - \pi^*)_1$ and $(\pi - \pi^*)_2$ transitions electronically correlate with the intra- and intermolecular interaction between the ammonium and the carboxylate anion groups.

The amino acids whose side chains possess the π-electron conjugated groups, imidazolyl (His), phenyl (phenylalanine (Phe)), indolyl (tryptophan (Trp)), and hydroxyphenyl (tyrosine (Tyr)), yield the characteristic spectral patterns in the FUV region. Figure 4.14 shows the FUV spectra of the acid and the anion forms of these amino acids ((a) His, (b) Phe, (c) Trp, and (d) Tyr). In comparison of the ε spectra determined from the present ATR method with those from transmission methods in the wavelength region from 200 to 300 nm [76, 77], the positions of the band maxima nearly match each other, but the ε values determined by the ATR method are smaller by 0.55 times. This disagreement of the molar absorptivities mainly comes from the different orders of the sample concentrations ($10^{-6} - 10^{-3}$ M for the transmission and 1–2 M for the ATR study).

For Phe and Tyr, the characteristic bands appear from 175 to 300 nm, which are mainly derived from the $\pi - \pi^*$ transitions of the phenyl and hydroxyphenyl groups of the side chains. The $\pi - \pi^*$ bands of the carboxyl groups are completely obscured within the $\pi - \pi^*$ bands of the side chains. From the absorption spectra of benzene and substituted benzenes [78, 79], the intense bands around 190 nm and the weak bands around 250 nm correspond to the symmetry-allowed $\pi - \pi^*$ transition (^{1}B) and the symmetry-forbidden $\pi - \pi^*$ transitions (^{1}L$_a$ and ^{1}L$_b$), respectively. By comparing the ^{1}B bands between the acid and anion forms, (1) the band positions
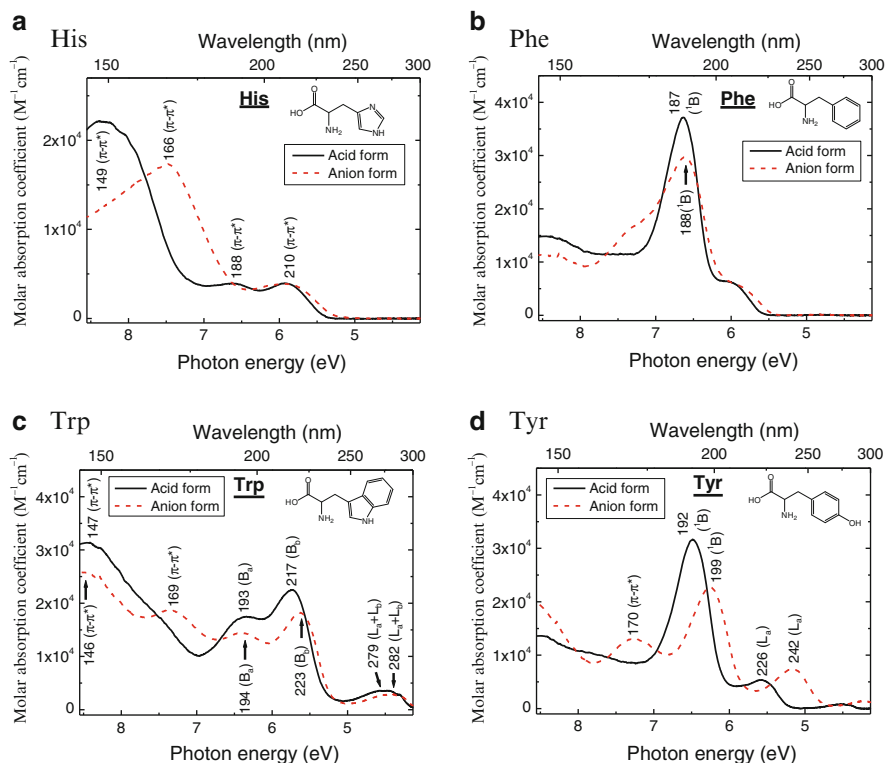
Fig. 4.14 FUV absorption spectra of ammonium carboxylic acid and aminocarboxylate anion forms of amino acids with aromatic side chain (**a**) His, (**b**) Phe, (**c**) Trp, and (**d**) Tyr (From Ref. [73])

of the acid forms stay at shorter wavelength than the anion forms, (2) the molar absorption coefficients of the acid forms are larger, and (3) the bandwidths of the acid forms are narrower. Those differences probably arise from the hydration strength of the amino acid molecules. The anion forms of the amino acids interact more strongly with the solvent water molecules than the acid forms.

The characteristic absorption bands of Trp spread over the entire FUV region, and those are mostly derived from the $\pi - \pi^*$ transitions of the indolyl group in the side chain. The $\pi - \pi^*$ transition of the carboxyl group is moderately obscured within the intense absorption of the indolyl group. The spectral changes upon protonation are relatively small, because the molecular structure of the side chain does not change with the proton concentrations. The bands around 193, 230, and 280 nm are assigned to the $\pi - \pi^*$ transitions to the B_a state, the B_b state, and the overlapping L_a and L_b states, respectively [80]. In comparison of the spectra among Phe, Trp, and Tyr, the electronic transition energies of the B bands decrease, and the molar absorption coefficients of the L bands increase for both the acid and anion forms due to the reduced benzene ring symmetry, as the benzene rings are more substituted from Phe to Trp.

4.5   Pulse Laser Photolysis of Aqueous Ozone in the Microsecond Range Studied by Time-Resolved Far-Ultraviolet Absorption Spectroscopy

Advanced oxidation processes (AOP) using aqueous ozone (O_3) with hydrogen peroxide (H_2O_2) and UV light irradiation have been widely employed to oxidatively destruct organic and inorganic contaminants in aqueous solution [81–84]. Even though O_3 has high reactivity to many chemical compounds, the reactivity to some compounds, such as alcohols and carboxylic acids, is quite small [85–87]. Hydroxyl radical (OH), which is a transient species from O_3 decomposition, possesses high reactivity to any target compounds [85–87]. The experimental conditions in the AOP processes were studied to efficiently generate OH at the target sites. However, the real-time monitoring of OH generation by the O_3 photolytic reaction in aqueous solution is not straightforward, because many transient species are short-lived (ns − ms), and their concentrations are relatively low.

FUV absorption spectroscopy is practical to analyze aqueous solutions quantitatively and qualitatively, because liquid water is optically transparent above 200 nm, and the most of organic and inorganic molecules have relatively strong optical absorptions corresponding to various types of electronic transition. The chemical species involved in the O_3 photolytic reaction also have characteristic FUV bands [88–92]. In order to analyze the chemical dynamics of the O_3 pulse-photolytic reaction in aqueous solution, we have developed a pump-probe nanosecond time-resolved FUV spectrophotometer using a nanosecond pulse laser (wavelength, 266 nm; duration, 10 ns) [93, 94]. From the measured spectra, the molar absorptivities (ε) and the concentration-time profiles of the constituted chemical species in the O_3 photolytic reaction can be estimated with a multivariate curve resolution (MCR) method [93]. The real-time monitoring of the constituted chemical concentrations is a basis for controlling the AOP quality in washing processes.

The transient absorption spectra of the O_3 aqueous solutions show the distinct changes upon the nanosecond pulse light irradiance. Figure 4.15 shows the time profiles of the transient absorbances of O_3 (78–480 μM) in 10 mM phosphoric buffer solutions ((a) pH 2.5, (b) 7.3, (c) 9.0, and (d) 11.3) from 190 to 225 nm. The transient absorbance is defined as *Transient* $Abs(t) = -\log(I(t)/I_0)$ where $I(t)$ is the signal of the probe light intensity and I_0 is the time-averaged signal before the pump light irradiation. Because the transient absorbance of O_3 in pure water (pH 4.7) is similar with that in the pH 5.2 buffer solutions, the effects of the phosphate anions on the O_3 pulse-photolytic reaction are negligible. The time at 0 s corresponds to the nanosecond pulse laser irradiation timing. For all the pH conditions, the transient absorbances decrease just after the pulse laser irradiation till 20 μs and become mostly stable between 20 and 50 μs. The decreases in the absorbances become larger and the time decay shorter, as the wavelength is longer. For pH 2.5, the absorbances at 20 μs are 0.014 and 0.095 for 190 and 225 nm, respectively. The time decay constants with single exponential (τ_1) are 3.8 and 1.0 μs for 190 and 225 nm, respectively. As pH increases, the decreases of the absorbances become small especially in the short wavelength region. For
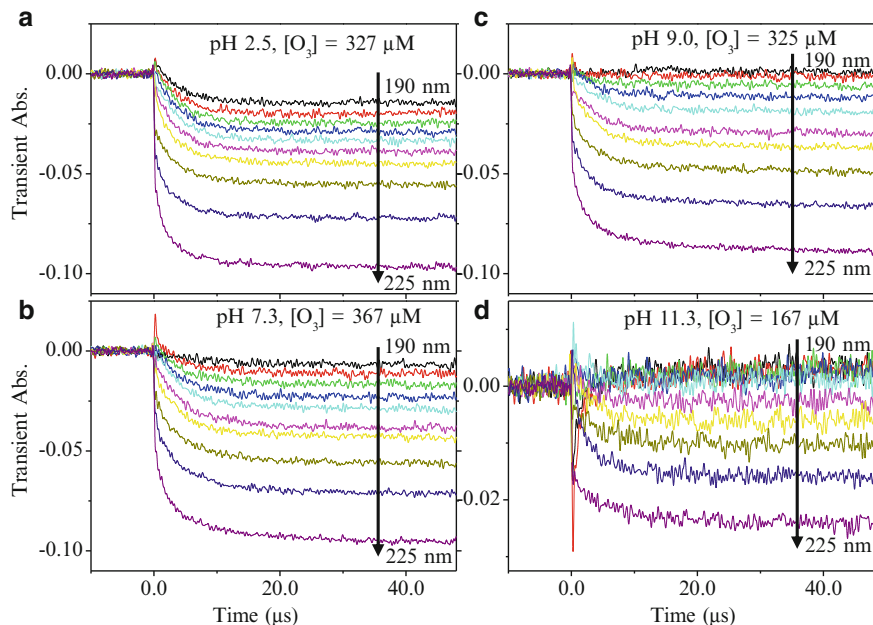
Fig. 4.15 Time profiles of the transient absorbance of O_3 in aqueous solutions at (**a**) pH 2.5, (**b**) 7.3, (**c**) 9.0, and (**d**) 11.3. The nanosecond laser pulses are irradiated at 0 s (From Ref. [93])

pH 11.3, the signal-to-noise ratio (SNR) of the transient absorbance is much lower than the other pH conditions, and the signals around 0 s highly fluctuate. This SNR degradation in the basic solutions indicates that the decomposition reaction of O_3 with OH^- lowers the O_3 concentration at the measurement position and increases the scattered light of the pump laser due to the formed O_2 bubbles. From the studies of stationary O_3 photolysis [95–99], the decreases of the transient absorbances in the longer wavelength region are mainly ascribed to the photodecomposition of O_3 and the increases in the shorter wavelength region to the formation of H_2O_2.

The measured transient spectrum matrix (**A**, time × wavelength channels) can be decomposed into the molar absorption coefficient matrix (**S**, wavelength × number of chemical species (n)) and the concentration-time profile matrix (**C**, time × n channels) based on Beer's law, as shown in the following equation [100]:

$$\mathbf{A} = \mathbf{CS}^{\mathrm{T}} + \mathbf{R} \tag{4.1}$$

The ε value of each chemical component involved in the O_3 photolytic reaction in aqueous solution (O_3, H_2O_2, OH, O_3^-, HO_2, O_2^-, and HO_2^-) was employed from the references [89–103] as the initial **S** matrices for alternating least-square fitting. The number of the constituted chemical components was determined as three, because the elements of the residual absorbance matrix (**R**) are completely random patterns along the time and the wavelength directions by applying three components: O_3, H_2O_2, and one of the transient chemical components. This analysis result indicates

that the contribution from other than the O_3 decomposition and the H_2O_2 formation can be described as the concentration change of one chemical component from the linear decomposition of the measured transient spectra. In order to distinguish which of the transient species (OH, O_3^-, HO_2, O_2^-, and HO_2^-) is the most probable as the third component, the MCR analyses were carried out in a way O_3 and H_2O_2 were always selected as the first and second components, and one of the transient species was selected as the third component. Then, the **S** and **C** matrices were calculated using each third component. To determine the most probable chemical species as the third component, the following conditions were applied to the calculated **C** matrices: (1) The concentration changes of H_2O_2 and the third component are not negative along the time, and (2) the concentration changes of H_2O_2 and the third component increase as the initial concentration of O_3 is higher. From the calculated **C** matrices, the probable third species that satisfy the above conditions are OH and HO_2.

The ε spectra ($\mathbf{S}_3$) of OH and HO_2 including wavelength region not reported in the references (190–225 nm) were determined from the following Eqs. (4.2) and (4.3) in order to evaluate which OH or HO_2 is more suitable as the third component contributing the changes in the transient absorbance.

$$\mathbf{A}_3 = \mathbf{A}_{\mathrm{exp.}} - \mathbf{S}_1\mathbf{C}_1 - \mathbf{S}_2\mathbf{C}_2 \tag{4.2}$$

$$\mathbf{S}_3 = \left(\mathbf{C}_3^{\mathrm{T}}\mathbf{C}_3\right)^{-1}\mathbf{C}_3^{\mathrm{T}}\mathbf{A}_3 \tag{4.3}$$

$\mathbf{A}_{\mathrm{exp.}}$ is the measured transient absorbance matrix, $\mathbf{C}_n$ is nth row of the calculated **C** matrix, and the columns of $\mathbf{S}_1$ and $\mathbf{S}_2$ are extended to 190 nm with the ε values of O_3 and H_2O_2 from the references. As the transient absorbance matrix **A** (time × wavelength channels) is not a square matrix, the calculated ε matrix $\mathbf{S}_3$ is a compromise solution. Figure 4.16 shows the calculated ε spectrum of each OH

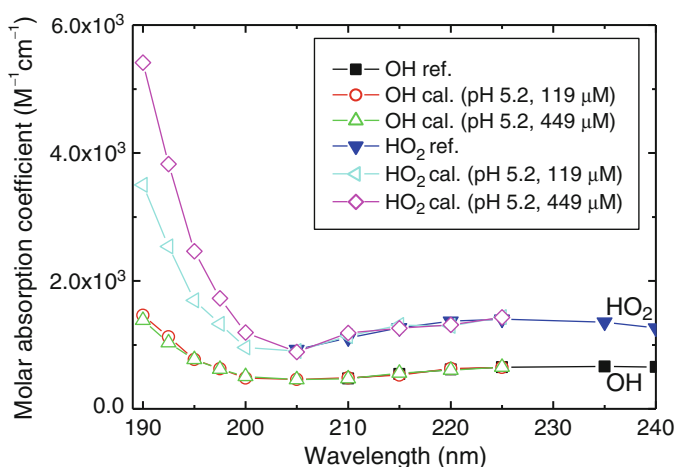**Fig. 4.16** Calculated ε spectra of OH and HO_2 extended to the shorter wavelength to 190 nm using Eqs. (4.2) and (4.3) and the ε values from the references [89, 103] (From Ref. [93])
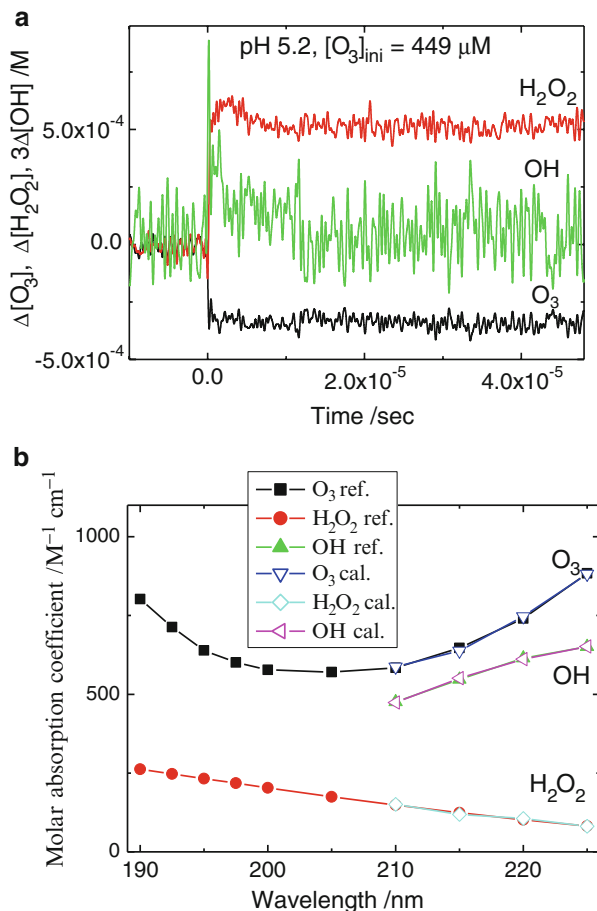
Fig. 4.17 Calculated **C** (**a**) and **S** (**b**) matrices from the transient absorbance ($[O_3]_{ini} = 449$ µM, pH 5.2) in the cases of OH as the third component and the ε values from the reference [89, 92, 103]. The concentration of OH was magnified by 3 times for clarity (From the reference [93])

and HO_2 in the region from 190 to 225 nm (OH cal., HO_2 cal.) with the reference spectra (OH ref., HO_2 ref.) [89, 103]. In the case of HO_2, the ε value below 205 nm increases as the initial concentration of O_3 is higher, while that of OH is mostly identical for all the initial concentrations of O_3. Thus, it can be said that OH is more suitable than HO_2 as the third component.

The decomposed **C** and **S** matrices reveal the chemical dynamics of the O_3 pulse-photolytic reaction in aqueous solution. Figure 4.17 shows the **C** (Fig. 4.17a) and **S** (Fig. 4.17b) matrices calculated from the time profiles of the transient absorbances at the condition ($[O_3]_{ini} = 449$ µM, pH 5.2) in the cases of OH as the third component. The vertical axis of Fig. 4.17a shows the concentration differences of O_3, H_2O_2, and

OH between before and after the pulse irradiation. The concentration change of OH (Δ[OH]) is magnified by 3 times for clarity. Upon the pulse laser irradiation, the O_3 concentration instantaneously decreases by 73 % from 449 to 120 μM for the first 0.3 μs, and then it becomes almost stable. The H_2O_2 concentration instantaneously increases to 550 μM for the first 0.3 μs and slightly increases further to 610 μM around 2 μs, and then it decreases to 460 μM around 20 μs. The OH concentration increases to 120 μM till 1 μs and gradually decreases to 20 μM till 20 μs, and then it remains stable after 20 μs. The examination of the chemical dynamics around 0 s is difficult, because the signal fluctuations due to the scattered light of the pump pulse laser cannot be completely removed. Figure 4.17b also shows the reference spectra of O_3, H_2O_2, and OH [89, 92, 103]. The calculated ε spectra of O_3, H_2O_2, and OH from S_3 match closely the reference spectra.

The present MCR analysis of the O_3 pulse-photolytic reaction becomes an important basis for real-time monitoring of chemical dynamics of AOP in washing processes with compact FUV spectrophotometers using optical filters.

References

1. D.J. Segelstein, http://www.philiplaven.com/p20.html
2. D.P. Stevenson, G.M. Coppinger, J.W. Forbes, J. Am, Chem. Soc. **83**(21), 4350–4352 (1961)
3. M. Halmann, I. Platzner, J. Phys. Chem. **70**, 580 (1966)
4. M.F. Fox, E. Hayon, J. Phys. Chem. **76**, 2703 (1972)
5. T.W. Marin, K. Takahashi, D.M. Bartels, J. Chem. Phys. **125**, 104314 (2006)
6. R.S. Mulliken, J. Chem. Phys. **3**, 506 (1935)
7. G. Herzberg, *Molecular Spectra and Molecular Structure III: Electronic Spectra and Electronic Structure of Polyatomic Molecules* (Van Nostrand, New York, 1966), p. 489
8. F. Williams, S.P. Varma, S. Hillenius, J. Chem. Phys. **64**, 154 (1976)
9. P.H. Hahn, W.G. Schmidt, K. Seino, M. Preuss, F. Bechstedt, J. Bernholc, Phys. Rev. Lett. **94**, 037404 (2005)
10. M. Rubio, L. Serrano-Andres, M.J. Merchan, Chem. Phys. **128**, 104305 (2008)
11. M. Chergui, N. Schwentner, Chem. Phys. Lett. **219**, 237 (1994)
12. K. Watanabe, M. Zelikoff, J. Opt. Soc. Am. **43**, 753 (1953)
13. P. Gurtler, V. Saile, E.E. Koch, Chem. Phys. Lett. **51**, 386 (1977)
14. A. Ikehata, Y. Ozaki, N. Higashi, J. Chem. Phys. **129**, 234510 (2008)
15. L.R. Painter, R.D. Birkhoff, E.T. Arakawa, J. Chem. Phys. **51**, 243 (1969)
16. G.D. Kerr, R.N. Hamm, M.W. Williams, R.D. Birkhoff, L.R. Painter, Phys. Rev. A **5**, 2523 (1972)
17. R.E. Verrall, W.A. Senior, J. Chem. Phys. **50**, 2746 (1969)
18. T. Shibaguchi, H. Onuki, R. Onaka, J. Phys. Soc. Jpn. **42**, 152 (1977)
19. K. Kobayashi, J. Phys. Chem. **87**, 4317 (1983)
20. R. Onaka, T. Takahashi, J. Phys. Soc. Jpn. **24**, 548 (1968)
21. T.I. Quickenden, J.A. Irvin, J. Chem. Phys. **72**, 4416 (1980)
22. A. Bernas, C. Ferradini, J.-P. Jay-Gerin, J. Photochem. Photobiol. A **117**(171) (1998)
23. F. Urbach, Phys. Rev. **92**, 1324 (1953)
24. A. Bernas, C. Ferradini, J.-P. Jay-Gerin, Chem. Phys. **222**, 151 (1997)
25. J.V. Coe, A.D. Earhart, M.H. Cohen, G.J. Hoffman, H.W. Sarkas, K.H. Bowen, J. Chem. Phys. **107**, 6023 (1997)
26. O. Christiansen, T.M. Nymand, K.V. Mikkelsen, J. Chem. Phys. **113**, 8101 (2000)

27. R. van Harrevelt, M.C. van Hemert, J. Chem. Phys. **114**, 9453 (2001)
28. Y. Miller, E. Fredj, J.N. Harvey, R.B. Gerber, J. Phys. Chem. A **108**, 4405 (2004)
29. D.M. Chipman, J. Chem. Phys. **122**, 044111 (2005)
30. P.C. do Couto, B.J.C. Cabral, J. Chem. Phys. **126**, 014509 (2007)
31. P.C. do Couto, D.M. Chipman, J. Chem. Phys. **137**, 184301 (2012)
32. M. Aschi, M. D'Abramo, C. Di Teodoro, A. Di Nola, A. Amadei, ChemPhysChem **6**, 53 (2005)
33. N. Higashi, A. Ikehata, Y. Ozaki, Rev. Sci. Instrum. **78**, 103107 (2007)
34. Y. Ozaki, Y. Morisawa, A. Ikehata, N. Higashi, Appl. Spectrosc. **66**(1), 1–25 (2012)
35. K.D. Collins, Biophys. J. **72**, 65 (1997)
36. B. Hribar, N.T. Southall, V. Vlachy, K.A. Dill, J. Am. Chem. Soc. **124**, 12302 (2002)
37. E. Vinogradov, P. Smirnov, V. Trostin, Russ. Chem. Bull. Int. Ed. **52**, 1253 (2003)
38. R.A. Robinson, R.H. Stokes, *Electrolyte Solutions* (Butterworth Scientific Publications, London, 1959)
39. G.A. Krestov, *Thermodynamics of Solvation* (Ellis Horwood, Chichester, 1991)
40. H. Ohtaki, N. Fukushima, J. Solut. Chem. **21**, 23 (1992)
41. V.I. Chizhik, A.V. Egorov, A.V. Komolkin, A.A. Vorontsova, J. Mol. Liq. **98–99**, 173 (2002)
42. W. Rudolph, M.H. Brooker, C.C. Pye, J. Phys. Chem. **99**, 3793 (1995)
43. T. Goto, A. Ikehata, Y. Morisawa, N. Higashi, Y. Ozaki, Phys. Chem. Chem. Phys. **14**, 8097–8104 (2012)
44. A. Ikehata, M. Mitsuoka, Y. Morisawa, N. Kariyama, N. Higashi, Y.J. Ozaki, Phys. Chem. A **114**, 8319–8322 (2010)
45. Y. Marcus, J. Chem. Soc. Faraday Trans. **87**, 2995 (1991)
46. C.K. Jørgensen, Spectroscopy of transition-group complexes, in *Advances in Chemical Physics*, ed. by I. Prigogine, vol. 5 (Wiley, Hoboken, 2007); ch 2
47. L.J. Nugent, J. Inorg. Nucl. Chem. **32**, 3485 (1970)
48. J. Kuta, A.E. Clark, Inorg. Chem. **49**, 7808 (2010)
49. M. Duvail, R. Spezia, P. Vitorge, ChemPhysChem **9**, 693 (2008)
50. J. Ciupka, X. Cao-Dolg, J. Wiebke, M. Dolg, Phys. Chem. Chem. Phys. **12**, 13215 (2010)
51. I. Persson, P. D'Angelo, S. De Panfilis, M. Sandström, L. Eriksson, Chem. Eur. J. **14**, 3056 (2008)
52. M. Seitz, A.G. Oliver, K.N. Raymond, J. Am. Chem. Soc. **129**, 11153 (2007)
53. P.G. Allen, J.J. Bucher, D.K. Shuh, N.M. Edelstein, I. Craig, Inorg. Chem. **39**, 595 (2000)
54. S. Goldman, L.R. Morss, Can. J. Chem. **53**, 2695 (1975)
55. D.F. Peppard, G.W. Mason, S. Lewey, J. Inorg. Nucl. Chem. **31**, 2271 (1969)
56. T. Goto, A. Ikehata, Y. Morisawa, N. Higashi, Y. Ozaki, Inorg. Chem. **51**, 10650 (2012)
57. T.C. William, The absorption and fluorescence spectra of rare earth ions in solution, in *Handbook on the Physics and Chemistry of Rare Earths*, ed. by K.A. Gschneidner Jr., L. Eyring, vol. 3 (Elsevier, Amsterdam, 1979); ch 24
58. K.B. Yatsimirskii, N.A. Kostromina, Theor. Exp. Chem. **2**, 436 (1966)
59. F.S. Richardson, M.F. Reid, J.J. Dallara, R.D. Smith, J. Chem. Phys. **83**, 3813 (1985)
60. N. Ishikawa, M. Sugita, T. Okubo, N. Tanaka, T. Iino, Y. Kaizu, Inorg. Chem. **42**, 2440 (2003)
61. M. Zbiri, M. Atanasov, C. Daul, J.M. Garcia-Lastra, T.A. Wesolowski, Chem. Phys. Lett. **397**, 441 (2004)
62. J. Hölsä, M. Karppinen, E. Kestilä, J. Alloys Compd. **207–208**, 65 (1994)
63. M. Atanasov, C. Daul, H.U. Güdel, T.A. Wesolowski, M. Zbiri, Inorg. Chem. **44**, 2954 (2005)
64. M. Kotzian, T. Fox, N. Rosch, J. Phys. Chem. **99**, 600 (1995)
65. M. Zbiri, C.A. Daul, T.A. Wesolowski, J. Chem. Theory Comput. **2**, 1106 (2006)
66. H.J. Svec, D.D. Clyde, J. Chem. Eng. Data **10**, 151 (1965)
67. I.P. Vinogradov, N.Y. Dodonova, Opt. Spectrosc. **30**, 14 (1970)
68. M. Tanaka, K. Yagi-Watanabe, F. Kaneko, K. Nakagawa, J. Phys. Chem. A **114**, 11928 (2010)
69. R. Abouaf, Chem. Phys. Lett. **451**, 25 (2008)
70. O. Plekan, V. Feyer, R. Richter, M. Coreno, M.D. Simone, K.C. Prince, V. Carravetta, J. Phys. Chem. A **111**, 10998 (2007)

71. P.A. Snyder, P.M. Vipond, W.C. Johnson, Biopolymers **12**, 975 (1973)
72. K. Matsuo, Y. Matsushima, T. Fukuyama, S. Senba, K. Gekko, Chem. Lett. **31**, 826 (2002)
73. T. Goto, A. Ikehata, Y. Morisawa, Y.J. Ozaki, Phys. Chem. A **117**, 2517–2528 (2013)
74. T. Fukuyama, K. Matsuo, K. Gekko, J. Phys. Chem. A **109**, 6928 (2005)
75. A. Osted, J. Kongsted, K.V. Mikkelsen, O. Christiansen, Chem. Phys. Lett. **429**, 430 (2006)
76. H. Nishino, A. Kosaka, G.A. Hembury, K. Matsushima, Y. Inoue, J. Chem. Soc. Perkin Trans. **2**, 582 (2002)
77. E. Mihalyi, J. Chem. Eng. Data **13**, 179 (1968)
78. J.R. Platt, H.B. Klevens, Chem. Rev. **41**, 301 (1947)
79. A. Bolovinos, P. Tsekeris, J. Philis, E. Pantos, G. Andritsopoulos, J. Mol. Spectrosc. **103**, 240 (1984)
80. J.A. Sweeney, S.A. Asher, J. Phys. Chem. **94**, 4784 (1990)
81. G.R. Peyton, W.H. Glaze, Environ. Sci. Technol. **22**, 761 (1988)
82. B. Meunier, A. Sorokin, Acc. Chem. Res. **30**, 470 (1997)
83. C.P. Huang, C. Dong, Z. Tang, Waste Manag. **13**, 361 (1993)
84. D. Bahnemann, E.J. Hart, J. Phys. Chem. **86**, 252 (1982)
85. J. Hoigné, H. Bader, Water Res. **17**, 173 (1983)
86. J. Hoigné, H. Bader, Water Res. **17**, 185 (1983)
87. J. Hoigné, H. Bader, W. Haag, J. Staehelin, Water Res. **19**, 993 (1985)
88. K. Sehested, J. Holcman, E. Bjergbakke, E.J. Hart, J. Phys. Chem. **86**, 2066 (1982)
89. G. Czapski, B.H.J. Bielski, Radiat. Phys. Chem. **41**, 503 (1993)
90. P. Pagsberg, H. Christensen, J. Rabani, G. Nilsson, J. Fenger, S.O. Nielsen, J. Phys. Chem. **73**, 1029 (1969)
91. S.O. Nielsen, B.D. Michael, E.J. Hart, J. Phys. Chem. **80**, 2482 (1976)
92. R.E. Buehler, J. Staehelin, J. Hoigne, J. Phys. Chem. **88**, 2560 (1984)
93. T. Goto, Y. Morisawa, N. Higashi, A. Ikehata, Y. Ozaki, Anal. Chem. **85**, 4500 (2013)
94. Y. Morisawa, N. Higashi, K. Takaba, N. Kariyama, T. Goto, A. Ikehata, Y. Ozaki, Rev. Sci. Instrum. **83**, 073103 (2012)
95. M.D. Gurol, A. Akata, AICHE J. **42**, 3283 (1996)
96. T. Garoma, M.D. Gurol, Environ. Sci. Technol. **39**, 7964 (2005)
97. W.H. Glaze, J.-W. Kang, D.H. Chapin, Ozone Sci. Eng. **9**, 335 (1987)
98. G. Wittmann, I. Horváth, A. Dombi, Ozone Sci. Eng. **24**, 281 (2002)
99. B. Soo Oh, K. Suk Kim, M. Gu Kang, H. Je Oh, J.-W. Kang, Ozone Sci. Eng. **27**, 421 (2005)
100. J. Jaumot, R. Gargallo, A. de Juan, R. Tauler, Chemom. Intell. Lab. Syst. **76**, 101 (2005)
101. E.J. Hart, K. Sehested, J. Holoman, Anal. Chem. **55**, 46 (1983)
102. G. Czapski, J. Phys. Chem. **68**, 1169 (1964)
103. C.S. Foote, J.S. Valentine, A. Greenberg, J.F. Liebman (eds.), *Active Oxygen in Chemistry*, 1st edn. (Chapman and Hall, London, 1995)